nature physics

ARTICLES

PUBLISHED ONLINE: 3 MARCH 2013 | DOI: 10.1038/NPHYS2560

Creation and dynamics of knotted vortices

Dustin Kleckner* and William T. M. Irvine*

Knots and links have been conjectured to play a fundamental role in a wide range of physical fields, including plasmas and fluids, both quantum and classical. In fluids, the fundamental knottedness-carrying excitations occur in the form of linked and knotted vortex loops, which have been conjectured to exist for over a century. Although they have been the subject of considerable theoretical study, their creation in the laboratory has remained an outstanding experimental goal. Here we report the creation of isolated trefoil vortex knots and pairs of linked vortex rings in water using a new method of accelerating specially shaped hydrofoils. Using a high-speed scanning tomography apparatus, we measure their three-dimensional topological and geometrical evolution in detail. In both cases we observe that the linked vortices stretch themselves and then deform—as dictated by their geometrically determined energy—towards a series of local vortex reconnections. This work establishes the existence and dynamics of knotted vortices in real fluids.

Whereas tying a shoelace into a knot is a relatively simple affair, tying a field, for example a magnetic field, into a knot is a different story: the entire space-filling field must be twisted everywhere to match the knot being tied at the core. This interplay between knots and the space they live in lies at the heart of modern topology; beyond the world of mathematics, there is a growing realization that knots in space-filling fields are an essential part of physical processes spanning classical and quantum field theories[1–3], liquid crystals[4,5], electromagnetism[6–8], plasmas[9–12], and quantum and classical fluids[13–17], with static knotted structures having been demonstrated in the nodal lines of weakly focused laser beams[8] and liquid crystals[4,5,18].

In fluid and fluid-like systems, there is a long-standing basis for suggesting that knottedness is a conserved physical quantity, and that corresponding knotted excitations should exist[9–16,19–23]. The relevant knottedness comes in different forms: for example, in plasmas, the magnetic field lines, which guide the flow of current, may form stable knots and links. In a classical or quantum fluid—where the emphasis is on the vorticity field—the prototypical knottedness-carrying excitations are knotted vortex loops, akin to smoke rings, but tied into knots. These vortex loops, in which all vorticity lines are concentrated, act as an organizing centre for the surrounding flow that in turn determines its evolution.

In an ideal (inviscid) fluid, lines of vorticity can never cross, and so the topology of vortex loops is preserved: knots stay knotted, and linked rings stay linked. In real fluids—even superfluids—the situation is more complicated, and linking can change through reconnection events, whose detailed dynamics are challenging to resolve in both theory and experiment. Although interest in knotted vortices in ideal fluids dates back to Lord Kelvin, who first realized their topological robustness[24], their conjectured role in dissipative flows has generated much further interest. Tangles of vortex lines—the sinews of turbulence[25]—offer insights into understanding flow and dissipation in hydrodynamics, and much interest lies in determining their temporal stability and the mechanism through which knots dissolve. One key issue is the extent and mechanism for the dissipation of helicity, which is a bulk measure of the knottedness and linkedness of the flow that has direct counterparts in many other physical systems, such as magnetic helicity in plasmas[11] or optical fields[6,7]. So far, experimental tests of these ideas have been hampered by the lack of methods for creating topologically non-trivial vorticity fields on demand.

Here, we report an experimental observation of topological vortices in the form of trefoil knots and linked pairs of rings, generated by the acceleration of specially shaped hydrofoils. We observe rapid vortex stretching for both linked and knotted vortices, which is not present in isolated vortex rings (unknots), even if they are strongly distorted. This stretching is accompanied by a change of vortex geometry to conserve energy, and this process drives the vortices towards a series of local reconnections. Ultimately, this results in a change of the vortex topology to a set of unlinked rings. The present work establishes the existence and dynamics of long-sought-after knotted vortex loops in experiment and offers a glimpse into their topological evolution, paving the way for the experimental study of knotted excitations in hydrodynamic systems, including turbulent flows and quantum fluids.

The evolution of a collection of vortex loops is far more subtle than ribbons tied into knots: vortex loops are inherently dynamical objects transported by a self-generated, space-filling, flow field. This flow field, $u(x)$, has the same form as the magnetic field generated by a current flowing around a wire with the same shape as the vortex core, where the equivalent of current is the circulation around a path enclosing the core: $\Gamma = \oint u \cdot \mathrm{d}l$. As long as no other vortices intersect the core, this circulation must be constant around the vortex loop and is generally conserved in time, owing to the Kelvin circulation theorem. (Strictly speaking, circulation is exactly conserved only for an inviscid fluid. However, it will generally be conserved in the presence of viscosity as long as the vortex cores do not touch[26]; this is true even when there is vortex stretching, which will alter the local energy and vorticity density.) In the limiting case of the vortex core being infinitely thin, each segment of the vortex line evolves primarily under the influence of neighbouring segments. In this local induction approximation (LIA), the velocity of a point on the filament depends only on the local radius of curvature of the filament, with more (less) curved segments moving faster (slower); generally this implies that non-circular vortices will continuously deform as they evolve. This approximation captures the qualitative evolution of shaped filaments[19,27] and in 1981, the existence, under the LIA, of a family of knotted vortex shapes that evolve without change of form, by propagating and rotating,

James Franck Institute, Department of Physics, The University of Chicago, Chicago, Illinois 60637, USA. *e-mail: dkleckner@uchicago.edu; wtmirvine@uchicago.edu.

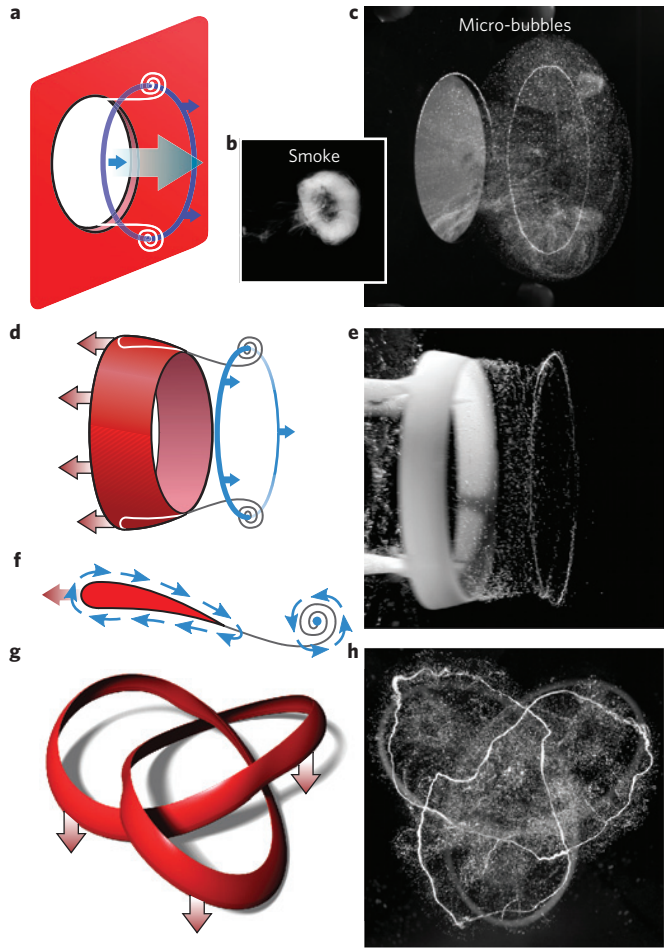

Figure 1 | The creation of vortices with designed shape and topology. **a**, The conventional method for generating a vortex ring, in which a burst of fluid is forced through an orifice. **b**, A vortex ring in air visualized with smoke. **c**, A vortex ring in water traced by a line of ultrafine gas bubbles, which show finer core details than smoke or dye. **d**,**e**, A vortex ring can alternatively be generated as the starting vortex of a suddenly accelerated, specially designed wing. For a wing with the trailing edge angled inward, the starting vortex moves in the opposite of the direction of wing motion **f**, The starting vortex is a result of conservation of circulation—the bound circulation around a wing is balanced by the counter-rotating starting vortex. **g**,**h**, A rendering of a wing tied into a knot (**g**), used to generate a knotted vortex (**h**).

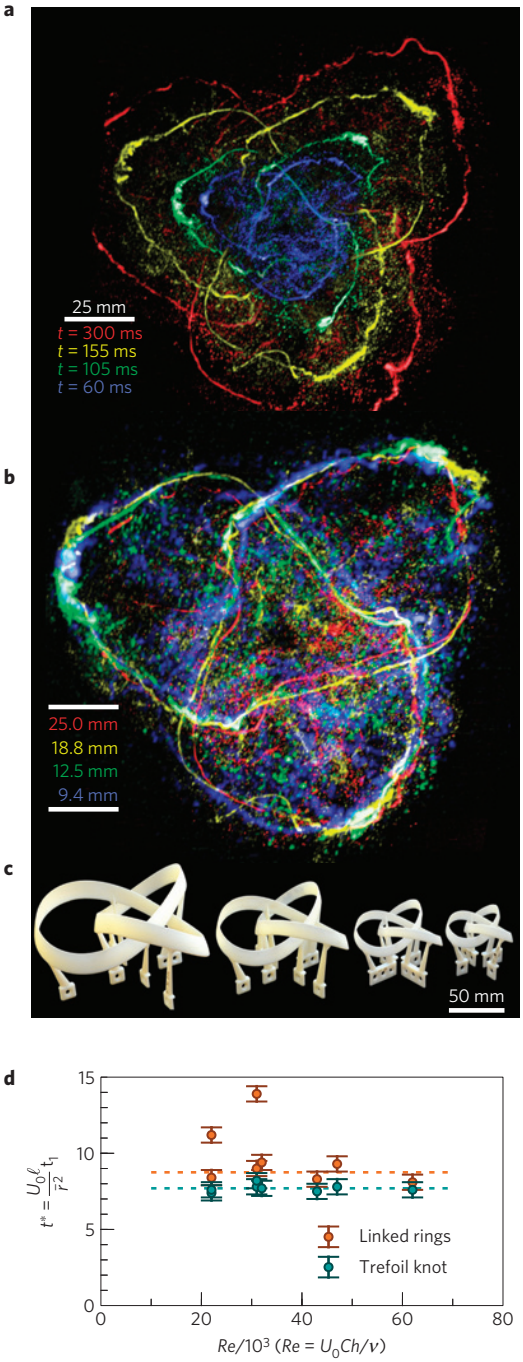

Figure 2 | Scaling of trefoil knot vortex loops. **a**, An overlay of vortex knots taken at the same rescaled time. The vortex r.m.s. radii are $\bar{r} = 60$, 45, 30 and 22.5 mm for red, yellow, green and blue colouring, respectively. The generating wing speed is 3.10 m s^{-1} for all except the largest vortex knot, for which it is 2.15 m s^{-1}. The biggest vortex (red) is slightly larger than the imaging field of view, resulting in some clipping on the left edge. **b**, The same knots as shown in **a**, scaled inversely proportional to the original hydrofoil dimensions. **c**, A photograph of the four knot-generating wings. **d**, The rescaled time, t^*, of the first reconnection event. With the exception of the smallest linked rings (which are affected by background flow from the apparatus), we observe that the rescaled reconnection time is independent of the Reynolds number.

was proved[20]. More recently, these solutions were shown to be unstable to linear perturbations[28]; however, when the LIA is no longer valid, the interplay of global and local induction complicates the situation considerably and the evolution of vortex knots remains a matter of theoretical debate both in the inviscid and viscid cases[21,22]. Simulations of knotted vortices with large cores, based on Navier–Stokes dynamics, suggest that they are short lived[29]; however, numerical integration of Biot–Savart vortex evolution suggests that finite core size may enhance stability[21]. Quantitatively, capturing the details of even the evolution of a simple ring remains a surprisingly resilient problem[30]. Resolving such subtle questions therefore requires both the generation of knotted flows in the laboratory, and an effective means of three-dimensional (3D) imaging of the evolution of the resulting flow with a high degree of spatial and temporal resolution.

The conventional method for making a vortex loop is to force a burst of fluid out of an orifice (Fig. 1a–c and Supplementary Movie S1). It has been suggested that two perturbed rings could be collided to create a knotted vortex[23], but to our knowledge this has never been demonstrated experimentally (our own attempts indicate that the strong perturbations to the shape of a vortex resulting from

the reconnection events make this difficult). As an alternative, we generate vortex loops based on the starting vortex shed by a suddenly accelerated wing (Fig. 1d,e and Supplementary Movie S2). A wing that is producing lift generates a flow that is faster on the top than the bottom. This can be represented as a superposition of a uniform background flow and a flow circulating around the wing. When this wing is suddenly accelerated from rest, the circulation created and carried by the wing is balanced by a second counter-rotating vortex line (Fig. 1f), close to the trailing edge of the wing[26].

We design hydrofoils (a wing designed for use in water) whose trailing edges trace the desired vortex shape. The tilt of the hydrofoil is kept constant everywhere except near the vicinity of crossing points (where the vortex lines overlap, as viewed from the front), where it is slightly reduced. The hydrofoils (Fig. 2c) are then fabricated using a 3D printer, and attached to a frame that is accelerated in a tank of water. The Reynolds number of our system is in the range 10^4–10^5, determined by the characteristic size of the hydrofoils, and the speed to which they can be smoothly accelerated (see Supplementary Methods for experimental details). A vortex knot produced by this method is shown in Fig. 1h and Supplementary Movie S3.

An experimental challenge in determining the topology of vortex lines is that it can be done only with 3D data. To image the core geometry, we use tiny ($\sim$100 μm) buoyant gas bubbles, which act as fine indicators for regions of high vorticity[31], without affecting the nature of the flow in our experiments. To reconstruct the bubbles trapped in the core in three dimensions, we scan a 1.5 W laser sheet over the experimental volume and record illuminated slices of the volume at 76,000 frames per second with a high-speed camera synchronized to the scanning motion. The 2D stream is converted to a volumetric data set of resolution 384 × 384 × 384 voxels (each approximately 400 μm cubed), spaced by 5.5 ms, sufficient to resolve the core evolution with considerable structural and temporal detail (see Methods for details).

Using the hydrofoil starting vortex method, we have successfully created two elemental topological vortices: trefoil knots and pairs of linked rings (Hopf links). As little is known analytically about the shape of stable vortex knots in fluids with non-zero viscosity, we chose the shape of our hydrofoils to match that of the invariant LIA solution for a trefoil knot, although departures from this shape did not qualitatively change the dynamics. The linked rings were shed from linked circular hydrofoils (see Methods for details). To test the generality of our approach, we compared the results of experimental runs with hydrofoils of different mean radii, $\bar{r}$, and accelerated to different speeds, U_0. Figure 2 shows the overlay of a range of trefoil vortex knots taken at the same rescaled time $t' = t \times (U_0 Ch/\bar{r}^2)$, and rescaled position $\boldsymbol{x}' = \boldsymbol{x} \times (1/\bar{r})$, where Ch is the chord of the hydrofoil (front to back length). After rescaling, the shape of our vortex loops, with a Reynolds number in the range $\sim 2 \times 10^4$–6×10^4, shows considerable overlap, demonstrating the robustness and repeatability of the approach.

Unlinked rings created using our starting vortex method behave as expected: circular rings simply move forward without changing shape (Supplementary Movie S2), and symmetrically distorted loops undergo regular oscillations (Supplementary Movies S4 and S5). The time evolution of trefoil knots and linked rings shows unexpected features (Fig. 3 and Supplementary Movies S6–S9). For both trefoil knots and linked rings, we observe that after an initial formation stage, the vortex loops propagate and rotate (for the trefoil knot, rotation is slower than LIA predictions: $\Omega \sim 0.5\Omega_{\mathrm{LIA}}$). However—crucially—the motion is not rigid: the vortices are observed to lengthen and deform towards a series of localized reconnections. Nearby regions of the vortex loop can be seen to approach one another, become nearly parallel, and twist around one another until they eventually collide (Fig. 3c and Supplementary Movies S10 and S11). After the resulting reconnection event, the vortex lines rapidly retreat, exciting prominent Kelvin waves (helical excitations of the vortex filament[32]) on the remaining vortex loops. This excitation modulates the core, propagating along it with a twisting motion. The deformation before the reconnection is reminiscent of the vortex bridging previously seen in simulations of vortex knots with large cores, where extended pairs of closely spaced counter-circulating vortex lines are observed before reconnections[29]. Ultimately, the result of the reconnections is that the topology of the vortices changes to a pair of unlinked rings. The separation between the resulting rings then increases as a function of time, with the front vortex having a smaller size and hence higher forward velocity (Fig. 4c,e).

Quantitatively, we use the rescaled time of the vortex reconnections as a measure of the lifetime of our linked vortices: $t^* = (U_0 Ch/\bar{r}^2)t_1$, where t_1 is the time of the first reconnection measured relative to the beginning of the hydrofoil acceleration (Fig. 2d). For a given geometry, we find that t^* varies minimally over the range of tested speeds and scalings, except for the smallest linked rings, $\bar{r} = 20$ mm; we attribute this to a disturbance created by the background flow from the acceleration frame.

Under the assumption that the vorticity is concentrated in thin cores that preserve circulation, the flow field and energetics can be reconstructed by tracing the core centreline. We use a fast-marching algorithm[33] to connect visually identified points along the core(s)[34], yielding their 3D coordinates. From the vortex geometry, the flow field outside the core can be calculated by the Biot–Savart law:

$$\boldsymbol{u}(\boldsymbol{x}) = \sum_i \frac{\Gamma_i}{4\pi} \oint_{C_i} \frac{\mathrm{d}\boldsymbol{r}_i \times (\boldsymbol{r}_i - \boldsymbol{x})}{|\boldsymbol{r}_i - \boldsymbol{x}|^3} \tag{1}$$

where Γ_i is the circulation of the vortex loop with closed core path C_i. Stream lines (integral lines of the flow field) are shown for several different vortex structures in Fig. 5. Similarly, the total energy of the vortex is given by:

$$E = \frac{\rho}{2} \sum_{i,j} \Gamma_i \Gamma_j \mathcal{E}_{ij} \tag{2}$$

$$\mathcal{E}_{ij} \simeq \frac{1}{4\pi} \oint_{C_i} \oint_{\substack{C_j \\ |r_i - r_j| > a/2}} \frac{\mathrm{d}\boldsymbol{r}_i \cdot \mathrm{d}\boldsymbol{r}_j}{|\boldsymbol{r}_i - \boldsymbol{r}_j|} + \delta_{ij} \frac{Y}{2\pi} \ell_i \tag{3}$$

where for each pair of vortex loops C_i and C_j, $\mathcal{E}_{ij}$ is the 'path inductance', which has units of length and is identical to the expression for the magnetic inductance of conducting wires with the same geometry, up to electromagnetic unit factors. The divergence in the self-inductance, $\mathcal{E}_{ii}$, is regularized by a short-range cutoff, $|r_i - r_j| > a/2$, identified with the vortex core radius, a, that leads to the second term, $(Y/2\pi)\ell_i$, where ℓ_i is the length of loop i and $Y \sim 1/4$ is a small dimensionless correction factor that depends on the core model[35] (see Supplementary Methods for calculation details). By providing a purely geometric measure of the vortex energy, the path inductance yields insights into the evolution of the shape of the vortex.

Figure 4f–h shows the total vortex loop lengths, ℓ, and total path inductance, $\mathcal{E}$, for a three-fold distorted ring, a trefoil knot and a pair of linked rings (for multiple vortices, we assume they have equal circulation Γ_i, and define $\mathcal{E} \equiv \sum_{i,j} \mathcal{E}_{ij}$ so that $E = (1/2)\rho\Gamma^2\mathcal{E}$). Significant differences are observed between the behaviour of linked and unlinked vortex structures. Perfectly circular vortex loops are essentially invariant in shape, and the length of the three-fold distorted ring oscillates by $\sim$5%. In contrast, the length of both the trefoil and linked rings increases markedly ($\sim$40%) as they approach reconnection events. Their corresponding energies depend on the core size, a, which we do not directly resolve. Accordingly, we calculate the self-energy (inductance) for both a range of constant core sizes (teal, Fig. 4f–h) and for a viscously diffusing core ($a = \sqrt{4\nu t}$, where $\nu = 1\,\mathrm{mm^2\,s^{-1}}$ is the kinematic

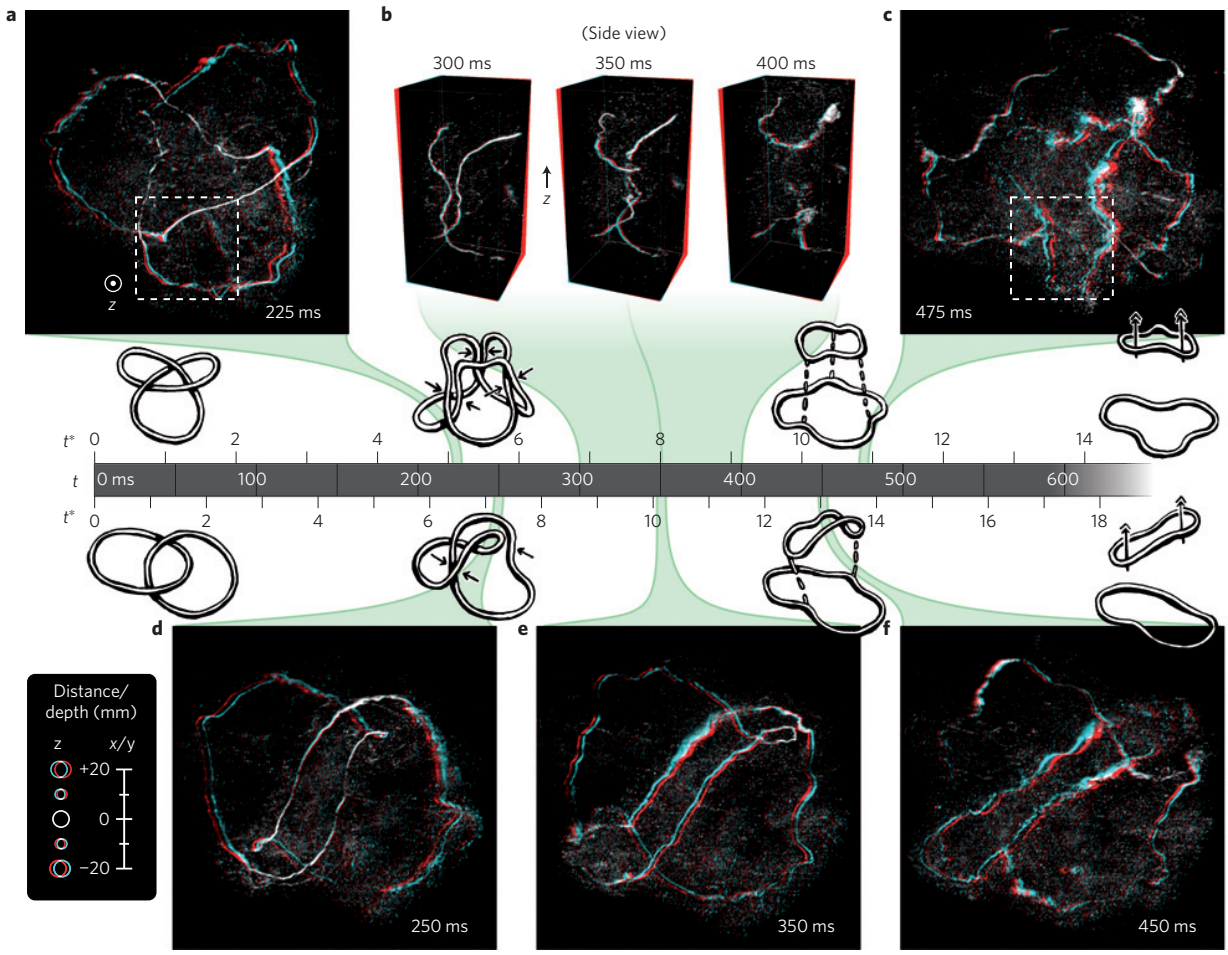

Figure 3 | Topological evolution of linked and knotted vortex loops in three dimensions. a–f, Reconstructed images of a trefoil vortex knot ($\bar{r} = 45$ mm; **a–c**) and a pair of linked rings (each with $r = 40$ mm; **d–f**), The large images (**a**,**c**,**d–f**) show the entire vortex structure as viewed from the front, and **b** shows three sub-images of a reconnection event for the trefoil knot, shown from the side (the shown sub-region is indicated with dashed lines in **a**,**c**). These images are designed to be viewed with red-cyan 3D glasses, but the depth of the vortex lines can also be determined from the provided scale bar (depth indicated with the circles at left). A timeline in the centre indicates the real and rescaled time, as well as indicating the topological evolution of the vortices.

viscosity of the fluid), shown in orange. The calculated energy for a circular or the three-fold distorted ring either varies minimally (for fixed core size) or decreases logarithmically (viscously diffusing core). Although the core size should increase owing to viscous diffusion, thereby reducing the total energy of the vortex loop, it does not change the core centreline dynamics apart from a slow (logarithmic) decrease in overall velocity.

For both knots and links, the path inductance, and hence energy, stays approximately constant despite the marked increase in length. To conserve energy, the lengthening process is associated with vortex bridging, where pairs of vortex lines in opposing directions approach one another; bridge regions decrease the total energy because the circulation is in opposite directions in the regions of close approach (in equation (3), $\mathrm{d}\boldsymbol{r}_i \cdot \mathrm{d}\boldsymbol{r}_j < 0$ for the bridges, reducing energy). For the linked rings, the quantitative effects of this shape change are captured by the mutual inductance of the two loops, $\mathcal{E}_{12}$, which is originally positive, but becomes negative as the bridges grow (Fig. 4h). Ultimately, as this overall vortex line stretching progresses, parts of the vortex loop will necessarily be driven more closely together, culminating in a reconnection event in the case of both linked rings and trefoil knots.

Following a reconnection, the tracer bubbles are considerably displaced, making it challenging for line-tracking algorithms to automatically track the vortex loop after they occur. However, for the case of the linked rings, we were able to track the core shape immediately following the first reconnection event (Fig. 4h), and observe almost no change in the path inductance. This apparent lack of dissipation in the reconnection event may be explained by the fact that the bridges have a much lower energy density than other regions of the vortex loop. On longer timescales, the excitation of Kelvin waves along the vortex filament, as seen in the raw data, leads to significant core disruption and may dissipate energy; the mechanics of these excitations will be the subject of future study.

The topological evolution of vortex knots observed in our system offers an experimental window into knotted excitations that are thought to occur in a wide range of continuous phases, such as plasmas[11], Bose–Einstein condensates[22], superfluids and other nonlinear fields[2,3]. As the topological dynamics are intrinsically geometric, our system provides a unique opportunity for experimentally probing many aspects of inherently dynamical knotted excitations that are difficult or impossible to observe directly in other physical systems. We note, for example, that the general reconnection sequence is similar to that seen in recent simulations of knotted vortices in Bose–Einstein condensates based on the nonlinear Schrödinger equation[22]. Furthermore, knots and links have been conjectured to appear in classical and superfluid turbulence, where their ephemeral structure makes them challenging to resolve.

A key question in all of these systems is the existence of an arrow of knottedness: the extent to which helicity, and hence the knottedness and linkedness of the field lines, is conserved. Do stable

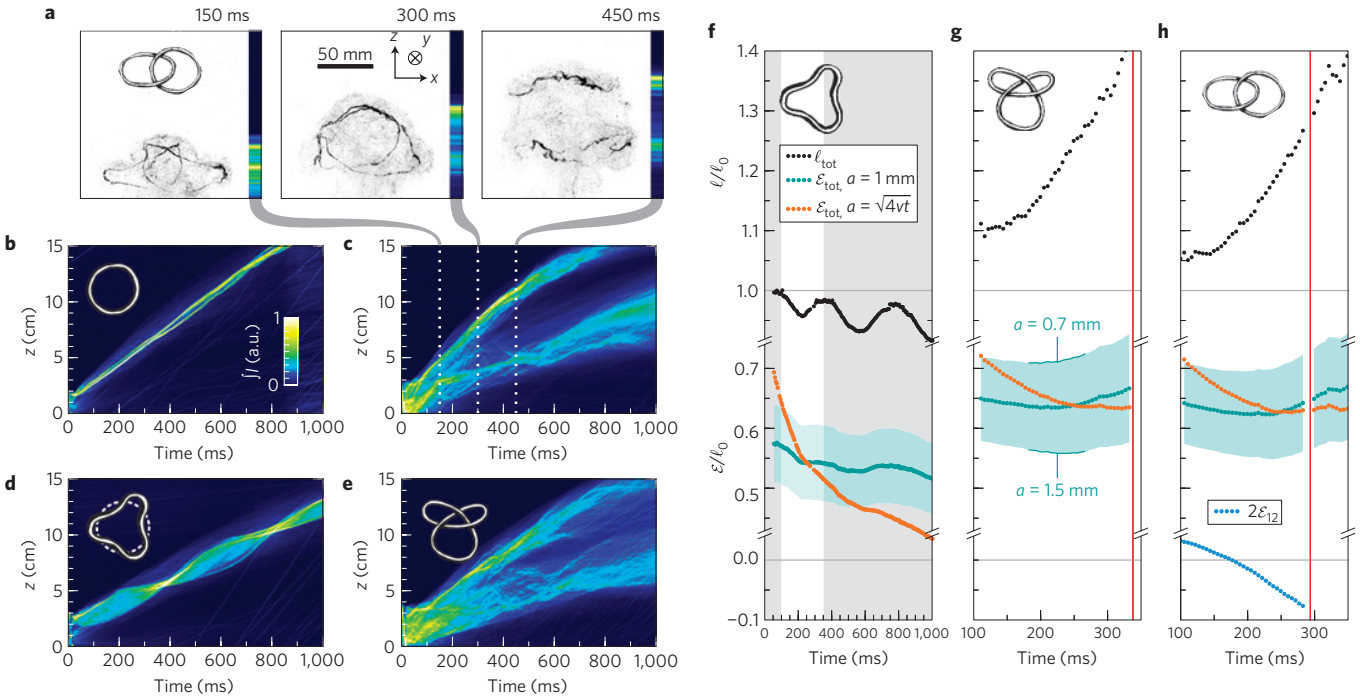

Figure 4 | Topological and energetic evolution of several types of vortex loop. a, Snapshots of a pair of linked vortex loops evolving at $t = 150$, 300, 450 ms, as viewed from the side. **b**–**e**, The integrated intensity as a function of z and t, for an unlinked ring (**b**), a pair of linked rings (**c**), a three-fold distorted ring (**d**) and a trefoil knot (**e**). In each case, the reconstructed 3D volume is integrated over x and y to show the evolution of the vortex in the primary direction of motion. For the **c**,**e**, the original linked structure is seen to evolve into two unlinked, distorted, rings of different size, which separate as a function of time. In **d**, the three-fold ring, distorts out of plane as it evolves, and shows shape oscillations with a half-period of ~400 ms. **f**–**h**, The length, ℓ, and total path inductance, $\mathcal{E}$, of a three-fold distorted ring (**f**), a trefoil knot (**g**) and a pair of linked rings (**h**), obtained from a core-tracing algorithm. A shorter time span is plotted for the linked structures (**g**,**h**); this corresponds to the unshaded region in **f**. The time of the first reconnection event (~300 ms) is shown as a red vertical line in **g**,**h**. The length (black) is seen to increase markedly for the linked and knotted vortices, but not for a three-fold distorted loop. The path inductance is shown both for a range of constant core sizes (teal: the centre dots are for 1 mm, and the filled region is 0.7–1.5 mm), and for a viscously determined core (orange, where $a = \sqrt{4\nu t}$ and $\nu = 1\,\mathrm{mm^2\,s^{-1}}$). For the linked rings (**h**) the mutual inductance, $\mathcal{E}_{12}$, is shown in blue; it does not depend on core size.

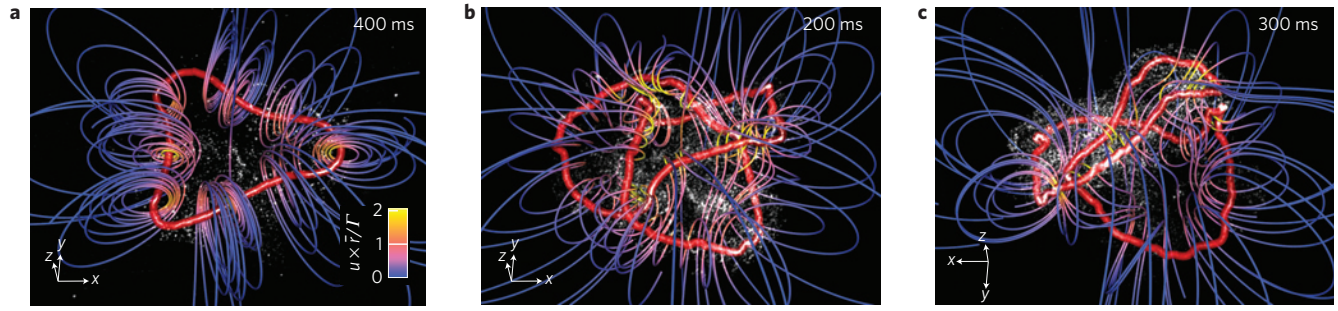

Figure 5 | Reconstruction of the vortex core and flow field from raw 3D data. a–**c**, The rendered data correspond to a three-fold distorted loop (**a**), a trefoil knot (**b**) and a pair of linked rings (slightly after the first reconnection event; **c**). For each, the raw tomography data (white) are shown superimposed with the traced core (red) and several instantaneous streamlines (blue to yellow, calculated from the traced core and equation (1)). All are shown on the same scale ($\bar{r} = 40$ mm for the three-fold distorted loop). Individual streamlines for the three-fold distorted loop (**a**) are nearly planar in the region around core. This is qualitatively different from the case for the linked and knotted structures (**b**,**c**) where the streamlines are observed to travel along the core as they circle it; this is attributable to the presence of helicity in the flow.

knot types or shapes exist? If helicity is wholly or partially conserved, what consequences does this conservation have on fluid kinetics? If not, what mechanisms lead to its irreversible dissipation? In the case of our linked and knotted vortices, the flow of helicity may be tracked by imaging twistedness of the core after a reconnection—a significant challenge for future experiments. The techniques introduced here make it possible to create and study the evolution of vortices with different topologies, for example, Borromean-like links or non-fibred knots. The observations of trefoil vortex knots and linked rings reported here offer a glimpse into the dynamics of isolated vortex knots, including topology-changing reconnections and their energetics, paving the way for the generation and exploration of these fascinating excitations of nature.

Methods

Hydrofoil fabrication. The hydrofoil models are generated using a Python script that creates a simple wing profile that has a trailing edge that traces the desired vortex geometry. Our reference wing profile (used for trefoil knots with

$\bar{r} = 45$ mm and linked rings with $\bar{r} = 40$ mm) has a chord of 15 mm with a maximum cross-section thickness of 2.5 mm tapering to 0.15 mm at the trailing edge (see Supplementary Methods for more information). The leading edge is always parallel to the direction of motion, and the trailing edge is bent to an angle of 15° with respect to the leading edge and acceleration direction. Near the vortex crossing points, the bend of the wing is reduced to 4° in a narrow region to minimize the disturbance from a hydrofoil passing through an existing vortex (see Supplementary Fig. S1b,c). To keep vortex forward velocity approximately constant, we scale the wing dimensions with the vortex size, with the exception of the smallest vortices, where it would be too fragile. The hydrofoil designs are fabricated with a commercial 3D printer (Objet Connex 350) using an ultraviolet-cured polymer (Objet VeroWhite).

As little is known analytically about the shape of stable vortex knots in fluids with non-zero viscosity, we chose the shape of our hydrofoils to match that of the invariant LIA solution for a trefoil knot[20], characterized by a dimensionless rotation rate: $\Omega_{\mathrm{LIA}} = \omega\bar{r}/v = 0.21$ (Supplementary Fig. S1b,d). We also tested departures from this shape in the form of torus knots with a similar aspect ratio; this did not qualitatively change the dynamics discussed below.

In the case of linked rings, the LIA provides no guidance because it neglects interactions between different vortices. Experimentally, however, vortex rings are known to interact strongly, for example, scattering off or repeatedly passing through one another[36]. The linked rings shown in Fig. 3b and Supplementary Movies S8 and S9 were shed from hydrofoils shaped into two circles, offset by their radius and rotated along the axis joining their centres by ±20° (Supplementary Fig. S1c,e). As with the knot, we found that slight modification of the ring arrangement did not qualitatively affect dynamics.

Imaging and 3D reconstruction. The bubbles used to image the vortex loops are created by electrolysis. To generate slices of the sample volume for 3D reconstruction, a 1.5 W, 532 nm ND:YAG laser is spread into fan with a cylindrical lens approximately 1 m away from the sample volume. This laser fan has a vertical spread of 8° full-width at half-maximum and is focused to ∼0.2 mm horizontal width in the experimental volume. Horizontal scanning is provided by a galvanometer near the cylindrical lens, which is driven by a sawtooth wave. This scanning is synced to a high-speed camera (Vision Research Phantom V1610) recording at 76,000 frames per second, resulting in a captured volume of 384 × 384 × 384 with a resolution of $\sim(400\,\mu\mathrm{m})^3$ per voxel (some frames are discarded in the scan turn-around time). The laser sheet scan amplitude is adjusted so that the voxels have an aspect ratio of 1 at the centre of the image. To enhance the scattering amplitude, the camera axis is angled approximately 10° to the laser sheet normal. The data are corrected for perspective effects and reconstructed using 4D viewing software written in Python.

Line tracing. To trace the geometry of our vortex loops, we use the fast-marching algorithm[33] to connect 5–20 visually identified points along the vortex loops. To precisely follow the vortex loops, we compute the shortest path between pairs of points with the constraint that the speed is proportional to the intensity of the original recorded data, which are slightly blurred to reduce noise. In the rare case that a section of the vortex loop becomes exactly aligned with the laser sheet or camera, rendering it dark and untraceable, the ends of the darkened region are marked by hand, and a straight line is used to connect these points. (The darkened regions must be nearly straight, or they would not remain dark, and so this does not seem to introduce any resolvable error in the length or path inductance calculation.) The resulting paths are perspective corrected after the line tracking is complete. This method is an adaptation of techniques used to map blood vessels in medical images[34]. For our data, the obtained paths are extremely reproducible as long as the vortex loop is reasonably well covered with bubbles; this primarily limits us to tracking the vortices only up to the reconnection events, which can significantly disrupt the core imaging.

Received 5 September 2012; accepted 18 January 2013; published online 3 March 2013

References

1. Witten, E. Quantum-field theory and the Jones polynomial. *Commun. Math. Phys.* **121,** 351–399 (1989).
2. Faddeev, L. & Niemi, A. Stable knot-like structures in classical field theory. *Nature* **387,** 58–61 (1997).
3. Manton, N. & Sutcliffe, P. M. *Topological Solitons* (Cambridge Univ. Press, 2004).
4. Smalyukh, I. I., Lansac, Y., Clark, N. A. & Trivedi, R. P. Three-dimensional structure and multistable optical switching of triple-twisted particle-like excitations in anisotropic fluids. *Nature Mater.* **9,** 139–145 (2010).
5. Tkalec, U. *et al.* Reconfigurable knots and links in chiral nematic colloids. *Science* **333,** 62–65 (2011).
6. Irvine, W. T. M. & Bouwmeester, D. Linked and knotted beams of light. *Nature Phys.* **4,** 716–720 (2008).
7. Irvine, W. T. M. Linked and knotted beams of light, conservation of helicity and the flow of null electromagnetic fields. *J. Phys. A* **43,** 385203 (2010).
8. Dennis, M. R., King, R. P., Jack, B., O'holleran, K. & Padgett, M. Isolated optical vortex knots. *Nature Phys.* **6,** 118–121 (2010).
9. Chandrasekhar, S. & Kendall, P. C. On force-free magnetic fields. *Proc. Natl Acad. Sci. USA* **42,** 1–5 (1956).
10. Woltjer, L. A theorem on force-free magnetic fields. *Proc. Natl Acad. Sci. USA* **44,** 489–491 (1958).
11. Berger, M. A. Introduction to magnetic helicity. *Plasma Phys. Control. Fusion* **41,** B167–B175 (1999).
12. Freedman, M. H. & Berger, M. A. Combinatorial relaxation of magnetic fields. *Geophys. Astrophys. Fluid Dynam.* **73,** 91–96 (1993).
13. Moffatt, H. K. Degree of knottedness of tangled vortex lines. *J. Fluid Mech.* **35,** 117–129 (1969).
14. Moffatt, H. K. Some developments in the theory of turbulence. *J. Fluid Mech.* **106,** 27–47 (1981).
15. Ricca, R. L. & Berger, M. A. Topological ideas and fluid mechanics. *Phys. Today* **49,** 28–34 (1996).
16. Barenghi, C. F. Knots and unknots in superfluid turbulence. *Milan J. Math.* **75,** 177–196 (2007).
17. Babaev, E. Non-Meissner electrodynamics and knotted solitons in two-component superconductors. *Phys. Rev. B* **79,** 1–6 (2009).
18. Bouligand, Y. Recherches sur les textures des états mésomorphes. 6 - Dislocations coins et signification des cloisons de Grandjean-Cano dans les cholestériques. *J. Physique* **35,** 959–981 (1974).
19. Kambe, T. & Takao, T. Motion of distorted vortex rings. *J. Phys. Soc. Jpn* **31,** 591–599 (1971).
20. Kida, S. A vortex filament moving without change of form. *J. Fluid Mech.* **112,** 397–409 (1981).
21. Ricca, R. L., Samuels, D. & Barenghi, C. Evolution of vortex knots. *J. Fluid Mech.* **391,** 29–44 (1999).
22. Proment, D., Onorato, M. & Barenghi, C. Vortex knots in a Bose–Einstein condensate. *Phys. Rev. E* **85,** 1–8 (2012).
23. Ricca, R. New developments in topological fluid mechanics. *Il Nuovo Cimento.* **32,** 185–192 (2009).
24. Thomson, W. On vortex atoms. *Phil. Mag.* **34,** 94–105 (1867).
25. Moffatt, H. K., Kida, S. & Ohkitani, K. Stretched vortices—the sinews of turbulence; large-Reynolds-number asymptotics. *J. Fluid Mech.* **259,** 241–264 (1994).
26. Acheson, D. J. *Elementary Fluid Dynamics* (Clarendon, 1990).
27. Saffman, P. G. *Vortex Dynamics* (Cambridge Univ. Press, 1992).
28. Calini, A., Keith, S. F. & Lafortune, S. Squared eigenfunctions and linear stability properties of closed vortex filaments. *Nonlinearity* **24,** 3555–3583 (2011).
29. Kida, S. & Takaoka, M. Reconnection of vortex tubes. *Fluid Dynam. Res.* **3,** 257–261 (1988).
30. Donnelly, R. J. Vortex rings in classical and quantum systems. *Fluid Dynam. Res.* **41,** 051401 (2009) 1–31.
31. Douady, S. & Couder, Y. Direct observation of the intermittency of intense vorticity filaments in turbulence. *Phys. Rev. Lett.* **67,** 983–986 (1991).
32. Thomson, W. *XXIV. Vibrations of A Columnar Vortex* 155–168 (Philosophical Magazine Series 5, Vol. 10, 1880).
33. Sethian, J. A. A fast marching level set method for monotonically advancing fronts. *Proc. Natl Acad. Sci. USA* **93,** 1591–1595 (1996).
34. Deschamps, T. & Cohen, L. D. Minimal paths in 3D images and application to virtual endoscopy. *Med. Image Anal.* **5,** 281–299 (2001).
35. Dengler, R. Self inductance of a wire loop as a curve integral. Preprint at http://arxiv.org/abs/1204.1486 (2012).
36. Oshima, Y., Kambe, T. & Asaka, S. Interaction of two vortex rings moving along a common axis of symmetry. *J. Phys. Soc. Jpn* **38,** 1159–1166 (1975).

Acknowledgements

The authors acknowledge useful discussions with J. Burton, P. M. Chaikin, E. Efrati, H. M. Jaeger, H. K. Moffatt, S. R. Nagel, M. Scheeler, T. Witten and W. Zhang. We acknowledge MRSEC Shared Facilities at the University of Chicago (DMR-0820054) for the use of their instruments. This work was supported by the National Science Foundation (NSF) Materials Research and Engineering Centers (MRSEC) Program at the University of Chicago (DMR-0820054). W.T.M.I. further acknowledges support from the A.P. Sloan Foundation through a Sloan fellowship, and the Packard Foundation through a Packard fellowship.

Author contributions

W.T.M.I. conceived and supervised research. W.T.M.I. and D.K. designed experiments and developed vortex generation and analysis techniques. D.K. developed the tomography apparatus and software, performed experiments and processed data. D.K. and W.T.M.I. analysed results and wrote the manuscript.

Additional information

Supplementary information is available in the online version of the paper. Reprints and permissions information is available online at www.nature.com/reprints. Correspondence and requests for materials should be addressed to D.K. or W.T.M.I.

Competing financial interests

The authors declare no competing financial interests.